Geometrical aspects of alpha dose rates from UO<inf>2</inf> based fuels

Radiation Physics and Chemistry 199 (2022) 110336

Contents lists available at ScienceDirect

Radiation Physics and Chemistry

journal homepage: www.elsevier.com/locate/radphyschem

Geometrical aspects of alpha dose rates from UO_2 based fuels

N.L. Hansson [a,*], M. Jonsson [b], C. Ekberg [a], K. Spahiu [a,c]

[a] Nuclear Chemistry / Industrial Materials Recycling, Chalmers University of Technology, SE-412 96, Gothenburg, Sweden
[b] School of Engineering Sciences in Chemistry, Biotechnology and Health, Department of Chemistry, KTH Royal Institute of Technology, SE-100 44, Stockholm, Sweden
[c] Swedish Nuclear Fuel and Waste Management Co., SE-101 24, Stockholm, Sweden

ARTICLE INFO

Keywords:
UO_2
Alpha particles
Radiolytic oxidation
Dose rate
Fuel cracks
Spherical geometry

ABSTRACT

Models for calculating dose rates of spherical particles as well as in fuel cracks are important for radionuclide source term estimations. Dose rates from UO_2 based fuels were calculated for planar, spherical, and crack geometries. The escape probability for α-particles in spherical UO_2 particles was derived as a continuous equation. The dose rate increased with increasing spherical radius due to the decreasing relative volume of the surrounding water layer. The model produced escape probabilities that were closely predicted by the theoretical derivation. It was shown that the dose rate in water filled fuel cracks with width smaller than the range of an α-particle led to dissolution rates that were lower per unit surface area.

1. Introduction

Accurate prediction of the reactive radiolysis product generation by the strong radiation field of the highly radioactive spent nuclear fuel is a key factor in the estimation of the radionuclide source term (Sattonnay et al., 2001). These radiolysis products can alter the oxidation state of the nuclear fuel UO_2 matrix surface, significantly increasing its solubility. Barrier failure in a deep geological repository is believed to be improbable during early time stages when β- and γ-radiation dominates the radiation field of the spent fuel. At the time when barrier failure is considered more probable, α-radiation will be the dominating type of radiation (Shoesmith, 2000).

Spent nuclear fuel contains cracks ranging from a few to tens of μm due to the large temperature gradients in the fuel during operation (Tribet et al., 2017)(and references therein). The dose rate can be locally altered due to a larger surface area irradiating the crack solution volume. This could modify the effect of radiolytic oxidation and is therefore an important phenomenon in the modelling of fuel dissolution in contact with groundwater.

Corrosion can occur preferentially at grain boundaries, causing fragmentation of the fuel and release of fuel grains (Shoesmith, 2000). Fine UO_2 particles in solution can also be formed at uranium metal waste sites (Gregson et al., 2011), at natural uranium deposits such as at Cigar Lake in Canada (Vilks et al., 1993), or as hot particles after severe nuclear accidents (Kashparov et al., 1996) or from nuclear weapons testing (Zheltonozhsky et al., 2001; IAEA, 2011). In the dose rate calculation of these particles, an accurate description of the spherical geometry is required. This geometry is also relevant for dose rate calculations of high temperature gas-cooled reactor (HTR) kernels in contact with water (Poulesquen et al., 2006). However, dose rates of spherical particles and in fuel cracks have not been extensively studied (Tribet et al., 2017; Mougnaud et al., 2015; Jansson et al., 1994; Siberry et al., 2021a).

In this work, the α-particle emission geometry in spherical particles was studied, and a simplified escape probability relationship with respect to emission depth was derived. The α-dose rates were modelled at the UO_2–H_2O interface of planar surfaces, spherical particles and in fuel cracks. The accuracy of empirical treatments of the average α-particle escape energy was investigated and compared to the model developed in this work.

2. Methods

2.1. Particle distribution

In order to accurately model α-decay and particle emission in the UO_2 matrix, an isotropic emission distribution must be implemented. An isotropic particle path distribution is generated by using Archimedes theorem (Shao and Badler, 1996), i.e., randomizing points on a $[-1,1] \times [0,2\pi]$ cylinder and calculating the inverse axial projection on the unit sphere. This leads to a uniform distribution on the unit sphere given that the points on the cylinder are uniformly generated (Shao and Badler, 1996). This distribution is achieved in the model by randomizing values

* Corresponding author.
E-mail address: nikhans@chalmers.se (N.L. Hansson).

https://doi.org/10.1016/j.radphyschem.2022.110336
Received 11 March 2022; Received in revised form 3 June 2022; Accepted 14 June 2022
Available online 17 June 2022

of z0 = [−1,1] and θ = [0, 2π] for each particle, which gives cartesian coordinates (x, y, z) after scaling with the maximum range of an α-particle in the UO_2 matrix, δ_{UO_2}:

$$x = \sqrt{1 - z0^2} \cdot \cos(\theta) \cdot \delta_{UO_2} \quad (1)$$

$$y = \sqrt{1 - z0^2} \cdot \sin(\theta) \cdot \delta_{UO_2} \quad (2)$$

$$z = z0 \cdot \delta_{UO_2} \quad (3)$$

Generating $3 \cdot 10^3$ particles on the surface of a unit sphere is shown to be well distributed as shown in Fig. 1.

In order to also simulate a random emission coordinate, the vertical z-component of the particle path vector is deceased by a random depth in the UO_2 matrix. For the planar geometry the system can be generalized, as only the emission depth affects the particle path, i.e., shifting the particle coordinates in x and y coordinates results in the same path vector and attenuation of the particle.

For the spherical geometry, the depth is defined radially, and direction with respect to the boundary of the UO_2 sphere in 3D space must be considered. The initial emission coordinate is therefore randomized through randomizing the x, y, and z coordinates and checking if the point ends up within the UO_2 particle sphere with radius R. (The algorithm is somewhat inefficient due to ~48% of the random points being discarded, however the points are well distributed.) In order to ensure that the initial emission coordinate as well particle path vectors are implemented correctly, comparison with a theoretically derived parameter such as the escape probability can be performed.

2.2. Spherical geometry

The geometry for an α-particle emitted in a UO_2 sphere can be described as two intersecting spheres with radii δ_{UO_2} and R respectively. The α-particle sphere represents all potential emission paths from the emission coordinate $(x_\alpha, y_\alpha, z_\alpha)$. The separation distance between the center of the UO_2 sphere and the emission coordinate is denoted d, ($0 \leq d \leq R$, as the α-particle is emitted inside the UO_2 sphere). This gives the equations of the spheres:

$$x^2 + y^2 + z^2 = R^2 \quad (4)$$

$$(x - d)^2 + y^2 + z^2 = \delta_{UO_2}^2 \quad (5)$$

The geometry of α-particles emitted inside a sphere of radius R is shown in Fig. 2.

The center of the circular intersection A_I of the two spheres is located

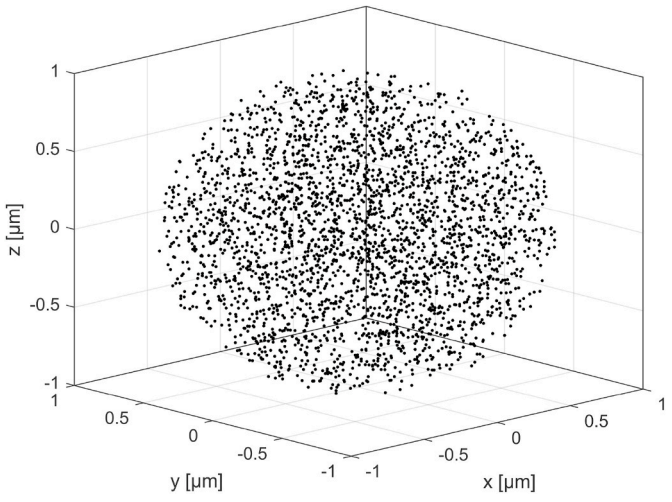

Fig. 1. Distribution of $3 \cdot 10^3$ particles randomly generated on the surface of a unit sphere using the Archimedes theorem.

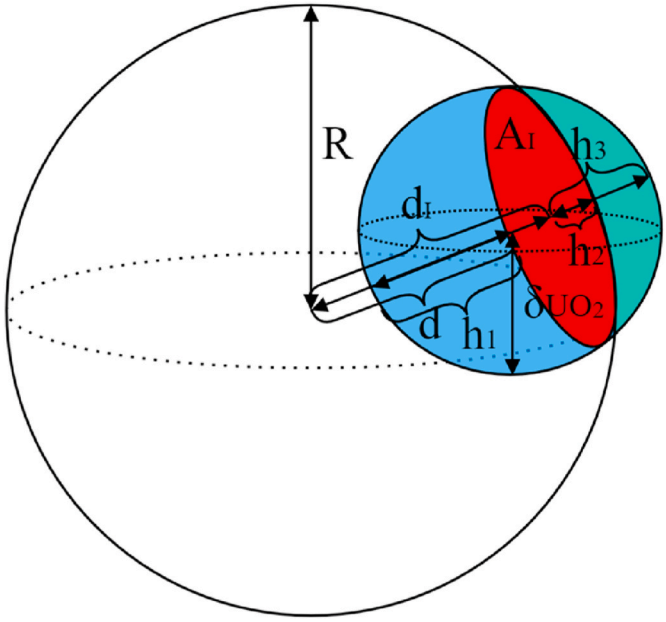

Fig. 2. 3D geometry of a UO_2 particle of radius R and α-particle emission sphere with radius δ_{UO2}, for the $R > \delta_{UO2}$ case. The circular intersection A_I is shown in red with a displacement d_I from the center of the UO_2-particle with resulting spherical cap heights h_1, h_2, and h_3.

at a displacement d_I from the center of the UO_2 sphere in the direction towards the α-particle sphere center. The value of d_I can be calculated as (Weisstein, 2007):

$$d_I = \frac{d^2 - \delta_{UO_2}^2 + R^2}{2d} \quad (6)$$

The spherical cap area of the α-particle sphere outside of the UO_2 sphere is calculated from the spherical cap height, h_3, which is defined outside of the center point of the circular intersection as shown in Fig. 2. The spherical cap heights h_1 and h_2 are calculated by (Weisstein, 2007):

$$h_1 = \delta_{UO_2} + d_I - d = \frac{(R - \delta_{UO_2} + d)(R + \delta_{UO_2} - d)}{2d} \quad (7)$$

$$h_2 = R - d_I = \frac{(\delta_{UO_2} - R + d)(\delta_{UO_2} + R - d)}{2d} \quad (8)$$

which allows for the cap height h_3 to be calculated:

$$h_3 = 2\delta_{UO_2} - h1 \quad (9)$$

The escape probability, $P(d)$, of an α-particle emitted in $(x_\alpha, y_\alpha, z_\alpha)$ is equal to the area of the spherical cap with height h_3, divided by the total surface area of the α-particle sphere (Nielsen and Jonsson, 2006):

$$P(d) = \frac{S_{cap,3}}{S_\alpha} = \frac{2\pi\delta_{UO_2} h_3}{4\pi\delta_{UO_2}^2} = \frac{h_3}{2\delta_{UO_2}} = 1 - \frac{h1}{2\delta_{UO_2}} \quad (10)$$

When the UO_2 sphere radius R is larger than the maximum α-particle range in the UO_2 matrix, i.e., $R > \delta_{UO_2}$, in order for the α-particle to have a potential escape path, the separation distance, d, must fulfill $d > R - \delta_{UO_2}$. This means that $P(d) = 0$ for separation distance $d < R - \delta_{UO_2}$. In the case of $R < \delta_{UO_2}$, $P(d) = 1$ for separation distances $d \leq \delta_{UO_2} - R$, since this case represents a full overlap of the two spheres with a larger α-particle emission sphere. It should be pointed out that the displacement, d_I, can assume negative values under these conditions (as expressed by Eq. (6)), as its direction is away from the center of the α-particle emission sphere, see Fig. 3b. Summarized, $P(d)$ can be expressed in terms of separation distance d as:

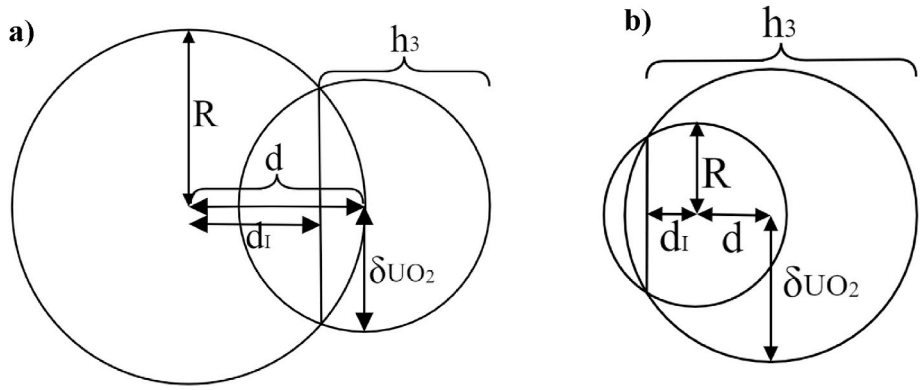

Figs. 3. 2d representations of the UO_2 particle of radius R and α-particle emission sphere with radius δ_{UO2} system. The spherical cap height h_3 is shown (**a**) to have a value larger than δ_{UO2} as the distance between the centers of the two spheres, d, is larger than the displacement of the intersectional plane, d_I. In the case of $\delta_{UO_2} > R$ (**b**), the displacement of the intersectional plane, d_I as well as d are added to the spherical cap height.

$$P(d) = \begin{cases} 1 - \dfrac{(R - \delta_{UO_2} + d)(R + \delta_{UO_2} - d)}{4\delta_{UO_2} d}, & |R - \delta_{UO_2}| < d \le R \\ 0 \quad , R > \delta_{UO_2},\ d \le R - \delta_{UO_2} & \\ 1 \quad , R < \delta_{UO_2},\ d \le \delta_{UO_2} - R & \end{cases} \tag{11}$$

In the work of Siberry et al. (2021a), the height of the spherical cap, h_3, is defined as:

$$h_3 = \delta_{UO_2} - |d_I - d| \tag{12}$$

which has a maximum value of δ_{UO_2}. As the value of $d_I - d$ becomes negative, i.e., in the case of the center of the α-particle sphere being located outside of the intersectional plane as shown in Fig. 3, the spherical cap height h_3 is larger than δ_{UO_2}. This behavior is not described by Eq. (12). This issue is however circumvented in the work of the authors as the spherical cap area is defined as piecewise function where for $d_I - d > 0$, the spherical cap area is calculated in accordance with the analysis in this work, and for values $d_I - d < 0$, the spherical cap area is calculated as $4\pi\delta_{UO_2}^2 - S_{cap,1}$. The piecewise functions given by the work of the authors can however be expressed as the continuous function given in Eq. (11) over the $|R - \delta_{UO_2}| < d \le R$ range if $d_I - d$ is allowed to assume negative values. This is shown for the $R > \delta_{UO_2}$ and $\delta_{UO_2} < R$ conditions using R = 50, 13 and 10 μm in Fig. 4, Fig. 5 & Fig. 6 respectively with the range of a 5.3 MeV α-particle in UO_2, $\delta_{UO_2} = 13.15$ μm. The piecewise functions given in the work of Siberry et al. (2021a) are shown for comparison. As shown in Fig. 5, the escape probability increases with very small values of d. This is due to the fact that close to the inner 0.15 μm of the UO_2 particle with radius R = 13 μm, the emission probability is 100% due to the range $\delta_{UO_2} = 13.15$ μm. α-particles emitted closer to the periphery of the UO_2 sphere can have a particle path inward, leading to a required escape particle path longer than the range of the α-particle, i.e., stopping the particle in the UO_2 matrix.

It is important to note that the emission depth, d, does not have an equiprobable distribution as the volume of layer at depth d is proportional to $(d^3 - (d - l)^3)$, where l is the layer size. This means that particles are more likely to be emitted in the outer layers of higher volume. For small values of l, the relative volume of the layers at depth d can be approximated by d^2. The layer volume weighted emission probability over the $|R - \delta_{UO_2}| < d \le R$ interval, P, can therefore be expressed as:

$$P = \frac{\int_{|R-\delta_{UO_2}|}^{R} \left(1 - \frac{(R-\delta_{UO_2}+d)(R+\delta_{UO_2}-d)}{4\delta_{UO_2} d}\right) d^2\, dd}{\int_{|R-\delta_{UO_2}|}^{R} d^2\, dd} \tag{13}$$

which describes the probability for a particle emitted in the $|R - \delta_{UO_2}| < d \le R$ interval to escape. The value of P in Eq. (13) approaches 25% with large values of R, as the surface approaches a planar geometry, e.g., for R = 10 mm, P = 25.03%.

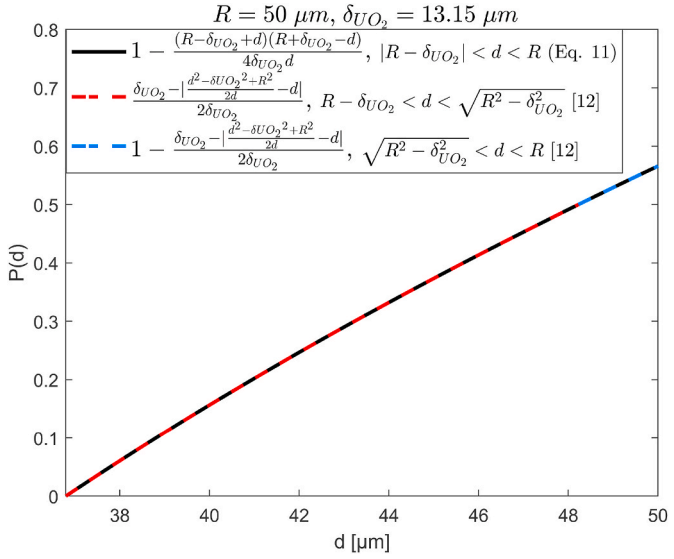

Fig. 4. The probability of α-particle escape as a function of emission distance, d, from the center of the UO_2 sphere with radius R = 50 μm. The equation for P (d) derived in this work is shown as the solid black line, and the dashed red and blue lines are the piecewise functions from the work of Siberry et al. (Siberry et al., 2021a).

2.3. Planar surface emission probability

Using spherical or polar coordinates to model the α-particle emission in the UO_2 matrix with polar and azimuthal angles, θ and φ, uniformly distributed between $[0, 2\pi]$ and $[0, \pi]$ respectively, the resulting angular distribution is non-isotropic due to a concentration of angles around the poles (Shao and Badler, 1996). The resulting mapping of the points is uniformly distributed on the surface of a cylinder and not a sphere. In a previous work of our group, this incorrect distribution of angles was generalized to 2D, yielding an escape probability of $1/\pi$ (Hansson et al., 2020). However, the time for the fuel material to emit n particles into solution was calculated from the number of emitted particles. This results in a normalization with respect to the escape probability, as an increased probability leads to a shorter emission time, thus cancelling the proportional effect of emission probability. However, the resulting particle paths might be influenced by the incorrect geometrical description. The theoretical escape probability of an α-particle emitted

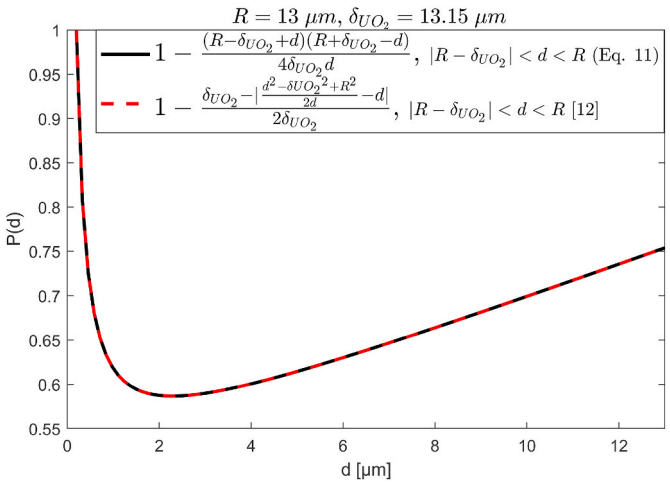

Fig. 5. The probability of α-particle escape as a function of emission distance, d, from the center of the UO_2 sphere with radius R = 13 μm. The equation for P (d) derived in this work is shown as the solid black line, and the dashed red line is the piecewise function from the work of Siberry et al. (Siberry et al., 2021a).

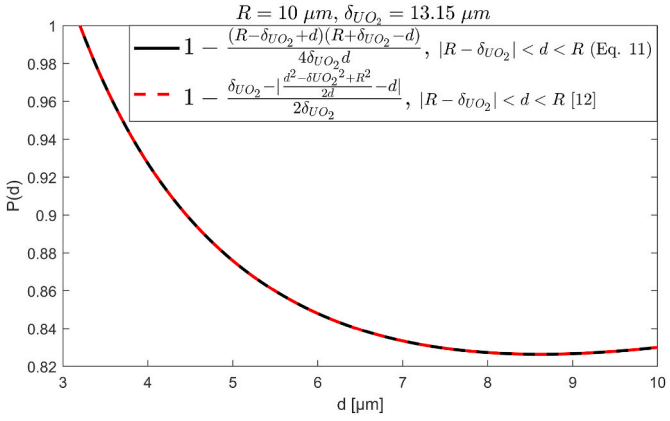

Fig. 6. The probability of α-particle escape as a function of emission distance, d, from the center of the UO_2 sphere with radius R = 10 μm. The equation for P (d) derived in this work is shown as the solid black line, and the dashed red line is the piecewise function from the work of Siberry et al. (Siberry et al., 2021a).

in a planar UO_2 source is a linear function of emission depth, *d*, as identified by Nielsen and Jonsson, and Siberry et al. (Nielsen and Jonsson, 2006; Siberry et al., 2021b):

$$P(d) = (\delta_{UO_2} - d) / 2\delta_{UO_2} \quad (14)$$

resulting in a linear escape probability of 50% and 0% respectively between $d = 0$ and $d = \delta_{UO_2}$, which corresponds well with Eq. (13).

2.4. Dose rate and dissolution rate calculation

The total activity of the UO_2 matrix is calculated through:

$$A_{tot} = S \cdot V \cdot \rho_{UO_2} \quad (15)$$

where *S* is the specific activity in units $Bq \cdot g^{-1}$, *V* is the volume of the UO_2 matrix in unit cm^3 and ρ_{UO_2} is the density of the UO_2 matrix in units $g \cdot cm^{-3}$. An arbitrary number of α-particles, *N*, are emitted in the UO_2 matrix, and the emission time of the particles is calculated as $t = N/A_{tot}$ in unit s. When modelling a planar surface a unit surface area is used, due to the dose rate being independent of the surface area. This is due to the fact that the surrounding water volume is scaled by the same factor if the surface area is changed.

The α-particles are stepwise attenuated from their emission point in the UO_2 matrix with a step size of 0.1 μm. In each step, the α-particles lose energy equal to the step size multiplied by the linear stopping power from ASTAR database (Toftegaard et al., 2014). (The ASTAR data can also be found in the ICRU 49 report (International Commission on Radiation Units, 1956).) The linear stopping power has to be updated after each consecutive step as it is dependent on the energy of the α-particle. The energy absorbed in the UO_2 and H_2O layers is stored in a vector with spatial resolution equal to the step size, in unit eV. The process continues until the particle has reached zero energy. The fraction of α-particles emitted in the UO_2 matrix escaping, as well as the individual energies of these particles when crossing the UO_2–H_2O interface, are kept track of. This allows for the average escape energy of the α-particles to be calculated. The escape probability produced by the stepwise isotropic emission model can be compared to the theoretical escape probability, to ensure that the step size and number of modelled particles lead to a sufficiently good resolution to reproduce the theoretical value.

The dose rate is calculated in unit $Gy \cdot h^{-1}$ through converting the absorbed energy vector into units J (conversion factor $1.602 \cdot 10^{-19}$ J/eV) and dividing by the weight of each layer as well as emission time. In the planar surface case, the weight of a layer is calculated through multiplying the surface area by the layer size and mass density. In the spherical geometry the weight of a layer is calculated through multiplying the volume of layer at depth *d* with layer size l by the mass density. Dose rate profiles for both the H_2O layer and UO_2 matrix are then obtained, the latter which is rarely included in dose rate models (Tribet et al., 2017; Mougnaud et al., 2015).

The absorbed energy vector is also used to calculate the H_2O_2 production rate in the water layers using the G-value for H_2O_2 of 0.985 molecules/100 eV (Christensen, 1998). Under an α-radiation field with a constant rate of H_2O_2 production and where the only consumption of H_2O_2 occurs through dissolution of UO_2, steady state is quickly reached. The dissolution rate of UO_2 then assumes the same rate as H_2O_2 production, which means that the resulting rate of oxidative dissolution is independent of the value of the oxidative dissolution rate constant under steady state (Jonsson et al., 2007; Nielsen et al., 2008).

3. Results and discussion

3.1. Planar interface dose rate

Modelling 10^6 α-particles emitted in the fuel specified in the work of Tribet et al., with an average α-particle energy of 5.3 MeV, a specific activity of $4.73 \cdot 10^8$ $Bq \cdot g^{-1}$ and a fuel density of 10.8 g cm^{-3}, with a step size of 0.1 μm, the dose rates in the UO_2 matrix and surrounding water layer are shown in Fig. 7. The resulting escape probability from the planar surface is 25% (0.2499), showing that the number of modelled particles as well as spatial resolution is sufficient to accurately predict the theoretical escape probability. The dose rate profiles at the solid liquid interface are similar to that of the 8 mm radius UO_2 particles modelled in the work of Tribet et al. The average dose rate in the closest 30 μm water layer is 919 Gy h^{-1}, which can be compared to the value obtained in the work of Tribet et al. of 791 Gy h^{-1} (Tribet et al., 2017). The 8 mm particle radius geometry can accurately be described as a planar surface, as the α-emitting particle volume to irradiated water volume ratio is practically identical compared to a planar surface, with an escape probability of ~25% (25.04% from Eq. (13)).

Previous works modelling dose rates in fuel cracks (Tribet et al., 2017; Mougnaud et al., 2015) as well as of spherical particles (Jansson et al., 1994; Siberry et al., 2021a) have often utilized empirical approximations in the analysis of their results. In the works of Mougnaud et al. (2015) and Tribet et al. (2017), dose rates in cracks and at liquid-solid interfaces of high level nuclear waste glass and spent nuclear fuel respectively are modelled. In the latter work, as well as in the work of Siberry et al. (2021a) the results are analyzed using the empirical relationship of average α-particle energies escaping from a planar UO_2

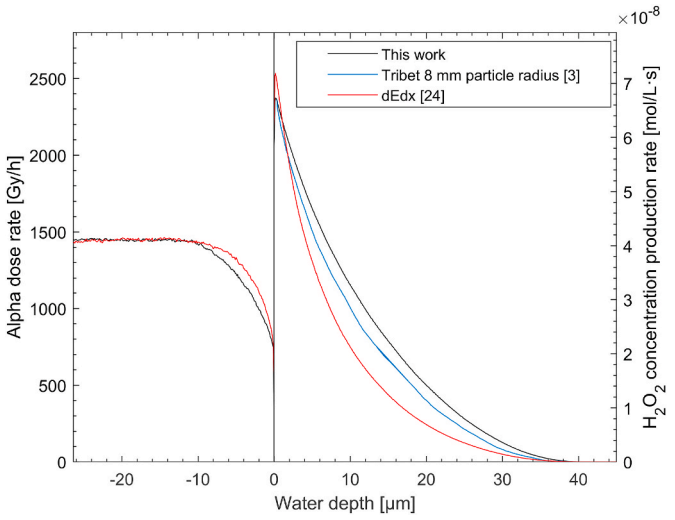

Fig. 7. UO_2–H_2O interface dose rate modelling the Tribet fuel with an average α-particle energy of 5.3 MeV and specific α-activity of $4.73{\cdot}10^8$ Bq·g^{-1} with mass density 10.8 g cm^{-3}. Comparison between dose rates from a spherical particle model with 8 mm radius in the work of Tribet et al. and a planar UO_2 surface studied in this work is shown. The comparison with the Nitzki and Matzke empirical stopping power in UO_2 is also shown.

surface derived by Garisto (1989):

$$E_{average} = \left(\frac{A}{2\delta_{UO_2}}\right)\left(\frac{2E_0^3}{3}+\frac{B}{A}E_0^2\right) \tag{16}$$

where E_0 is the initial emission energy, δ_{UO_2} is the maximum range of an α-particle with emission energy E_0 in the UO_2 matrix, and A and B are constants (Nitzki and Matzke, 1973). These constants are derived from the empirical description of the stopping power in the 2–8 MeV α-particle energy range in the work of Nitzki and Matzke in the form of (Nitzki and Matzke, 1973):

$$dE \,/\, dx = (AE+B)^{-1} \tag{17}$$

The average escape energy using the model developed in this work is 2.89 MeV, compared to the value of 2.62 MeV obtained from the Garisto empirical equation with A = 0.358 μm MeV^{-2}, B = 1.2 μm MeV^{-1}, using the range δ_{UO_2} = 13.2 μm (Tribet et al., 2017).

The reason for the underestimation of the average escape energy in the Garisto empirical equation is that it is derived from the approximate relationship in work of Nitzki and Matzke, which was derived from a stopping power fit over the 2–8 MeV energy interval (Nitzki and Matzke, 1973). As most of the Bragg-peak is not covered (Ziegler et al., 2010), it's evident that the stopping power values are significantly overestimated towards the lower end of the energy range. This is shown in Fig. 8, with mass stopping powers obtained from the ASTAR and SRIM databases together with the Nitzki and Matzke empirical equation for UO_2 mass stopping over the 0–5.3 MeV energy range. Mean values of the stopping powers over the energy range are also shown to highlight the overestimation of the Nitzki and Matzke relationship if applied to the whole energy range. It is therefore questionable if using the approximate relationship is suitable when making predictions on the overall α-particle attenuation behavior, such as in the average escape energy empirical equation derived by Garisto (1989). Using the mass stopping power relationship for α-particles in UO_2 derived by Nitzki and Matzke, as compared to the ASTAR stopping powers, modelling the aforementioned Tribet fuel yields a shorter α-particle range in the UO_2 matrix, of 11.9 μm. Additionally, a lower average α-escape energy of 2.33 MeV and an averaged dose rate over the inner 30 μm water layer of 674 Gy h^{-1} is obtained, as shown in Fig. 7 (red line), which demonstrates the impact of the overestimated stopping powers.

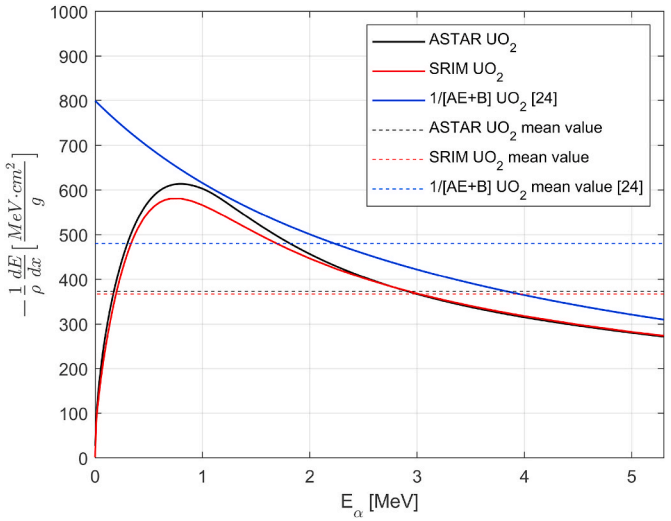

Fig. 8. Mass stopping powers in the 0–5.3 MeV α-particle range using the ASTAR and SRIM data bases and the empirical stopping power equation obtained from the work of Nitzki and Matzke (Nitzki and Matzke, 1973).

3.1.1. *Influence of particle energy on planar interface dose rate*

An increase in α-particle energy increases the energy deposited per UO_2 and H_2O layer as well as the averaged dose rate in the irradiated solution. As the dose rate is directly proportional to the specific activity of the fuel, the dose rate dependence of α-particle energy can be expressed as the dose rate to specific α-activity ratio. Using the dose rate model developed in this work, the resulting relationship when modelling a fuel with mass density 10.8 g cm^{-3}, shows a clear linearity between the dose rate in units Gy/h and the specific alpha activity in units MBq/g, see Fig. 9:

$$\dot{D} = S{\cdot}(0.269 \cdot E_\alpha - 0.009) \tag{18}$$

3.1.2. *Highly doped MOX fuel*

The 24 wt% Pu-doped fuel studied in previous works by our group (Hansson et al., 2020; Bauhn et al., 2018), with a specific α-activity of 4.96 GBq·g^{-1}, an average α-particle energy of 5.44 MeV and a density of 10.31 g cm^{-3} was modelled, and the H_2O-UO_2 interface profile is shown in Fig. 10. The average dose rate over the inner 43.5 μm water layer is 7.26 kGy h^{-1}. This value is 16% lower than the one in the previous study

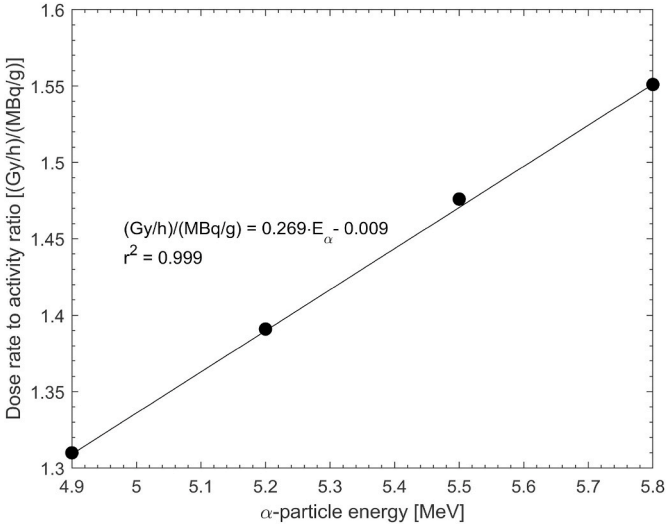

Fig. 9. Average dose rate to specific activity ratio as a function of α-particle emission energy using the dose rate model developed in this work.

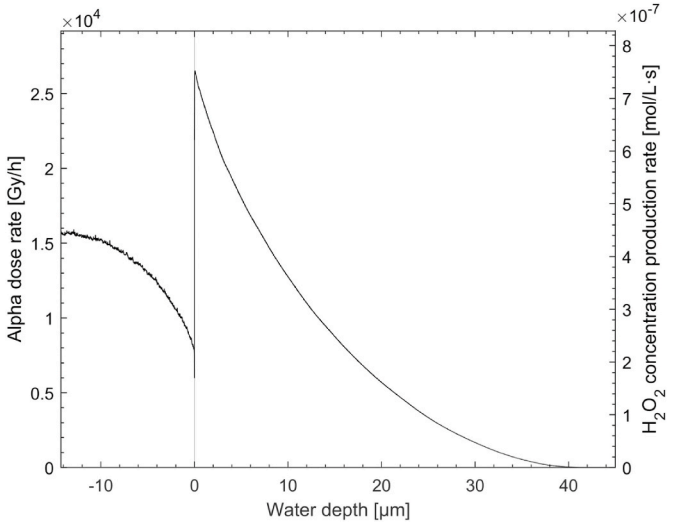

Fig. 10. UO_2–H_2O interface dose rate for a 24 wt% Pu-doped MOX fuel with α-particle energy of 5.44 MeV, specific α-activity of 4.96 GBq·g^1 and a mass density of 10.31 g cm^{-3}.

of Hansson et al., of 8.70 kGy h^{-1} (Hansson et al., 2020). The previous geometrical error (as discussed in section 2.3) therefore contributes to a noticeable effect due to the α-particle path distribution. Both studies are a significant improvement from the higher estimation of the 24 wt% Pu-doped fuel in the work of Bauhn et al. of 22.7 kGy h^{-1} which was calculated using the Sunder method (Bauhn et al., 2018; Sunder, 1998), as previously discussed in detail (Hansson et al., 2020).

3.2. Crack dose rate

The dose rate profile in a 25 μm water depth parallel crack modelling the Tribet fuel yields an average dose rate of 2.13 kGy h^{-1} as shown in Fig. 11a. The average dose rate over a crack as a function of crack width modelling the Tribet fuel is shown Fig. 11b, together with an exponential fit. The average dose rate is shown to be quite a strong function of the crack width.

In fuel cracks of width smaller than the range of an α-particle in H_2O, the total deposited energy in the crack water is strongly dependent on the crack width. Steady state dissolution rates modelling the Tribet fuel in cracks of width 1–43 μm, are shown in Fig. 12. The increased dose rate in the crack leads to a higher H_2O_2 production per unit volume. However, in a crack with width narrower than the range of an α-particle in water, more α-particle energy is absorbed in the UO_2 matrix, leading to a lower overall H_2O_2 production. The increased total deposited energy in the crack with increasing crack width therefore contributes to the higher steady state dissolution rate per unit surface area (mol·m^{-2}·s^{-1}). As the

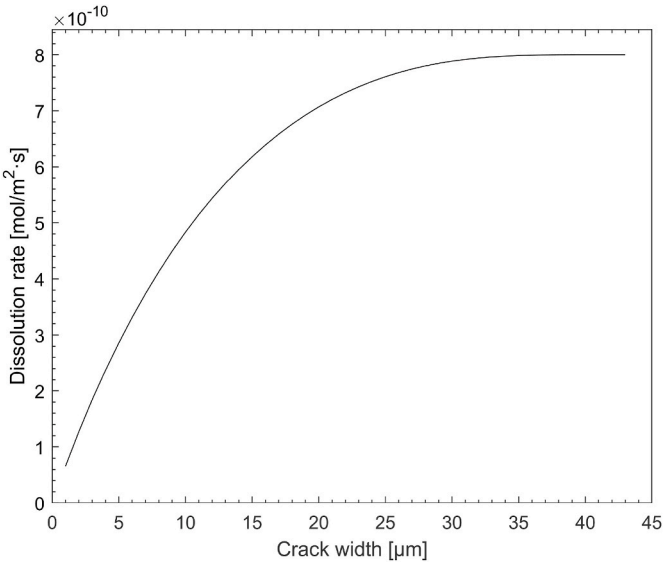

Fig. 12. Area-specific UO_2 dissolution rates modelling the Tribet fuel with α-particle energy of 5.3 MeV, specific activity of 4.73·10^8 Bq·g^{-1} and a fuel density of 10.8 g cm^{-3} with UO_2 crack width 1–43 μm.

crack width approaches the range of an α-particle in water, the dissolution rate per unit surface area approaches a constant value equal to that of a planar UO_2–H_2O interface.

3.3. Spherical geometry dose rate

The escape probability using Eq. (13) for $R = 50$ μm and $\delta_{UO_2} = 13.15$ μm gives $P = 0.3270$. With a relatively rough layer size of 1 μm, the difference in P calculating the layer volume as $(d^3 - (d-l)^3)$, deviates by less than 0.1%. The d^2 weight can therefore be used without loss of accuracy. The volume from which α-particles can escape in the $R = 50$ μm, $\delta_{UO_2} = 13.15$ μm sphere is 60% (0.5997). The total emission volume escape probability, i.e., the probability that an α-particle emitted in the sphere escapes, is consequently 19.83%. This is somewhat higher than the value of 16% achieved using the MCNPX source code in the work of Tribet et al. as discussed in the work of Siberry et al. (Tribet et al., 2017; Siberry et al., 2021a). The difference in average α-particle escape energy combined with the lower particle escape probability accounts for almost the entire difference in dose rate between the two works.

The dose rate profiles of spherical UO_2 particles with varying radius are shown in Fig. 13. The increasing dose rates with increasing particle radius are due to the decreasing water volume surrounding the UO_2 surface in relation to the particle size. With increasing radius, the

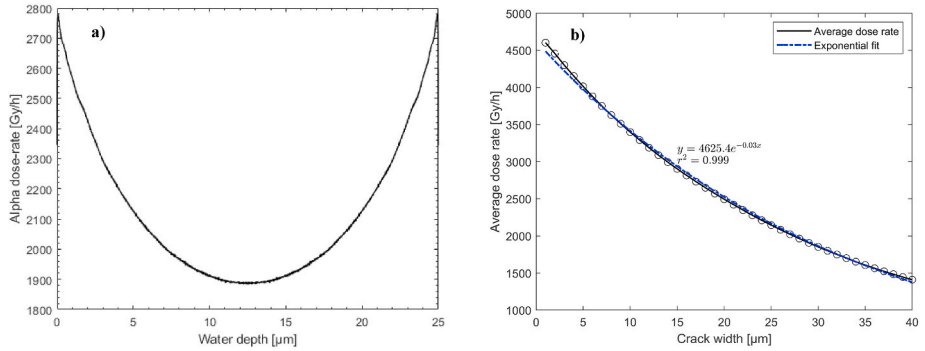

Fig. 11. α dose rate in a 25 μm water depth crack (a) as well as the average α dose rate over cracks with width 1–40 μm (b) together with an exponential fit, modelling the Tribet fuel with an α-particle energy of 5.3 MeV, specific activity of 4.73·10^8 Bq·g^{-1} and a fuel density of 10.8 g cm^{-3}.

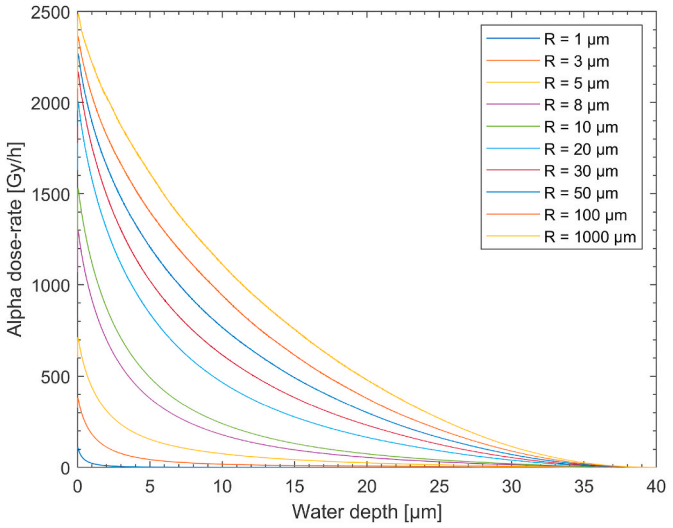

Fig. 13. Comparison between dose rates from spherical particles with radius R 1–1000 μm modelling the Tribet fuel with 5.3 MeV and specific α-activity of $4.73{\cdot}10^{8}$ Bq·g^{-1} with mass density 10.8 g.

α-particles are consequently distributed in a smaller water volume with respect to particle volume. The escape probability calculated from the model using $R = 50$ μm is calculated as $P = 0.3257$, for 10^6 particles with step size 0.1 μm, showing a small discrepancy compared to the theoretically predicted value.

Comparison of the dose rate in the current work and the one in the work of Siberry et al. modelling the Tribet fuel for a spherical UO_2 particle with radius 50 μm is shown in Fig. 14 (Siberry et al., 2021a). The average dose rate achieved from the model in this work is notably higher, 663 Gy h^{-1} compared to the average dose rate of 564 Gy h^{-1} in the work of Siberry et al. over the inner 30 μm water layer. This is likely due to the higher escape energy of the α-particles from the model in this work, as the escape energy from the 50 μm radius particle is reported as 2.47 MeV in the work of Siberry et al. This escape energy is significantly lower than the value of 2.95 MeV obtained in this work for the 50 μm particle radius. The relative difference in average escape energy corresponds well with the difference in dose rates, suggesting that the authors might be overestimating the attenuation in the UO_2 matrix,

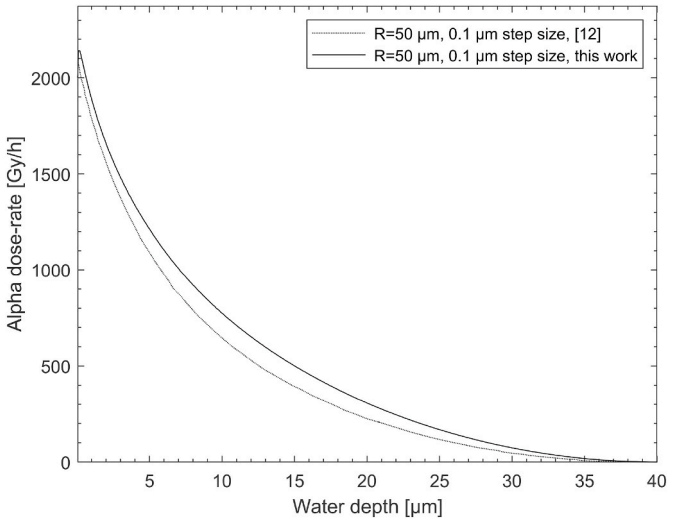

Fig. 14. Comparison between dose rates from spherical particles with radius 50 μm in the work of Siberry et al. (Siberry et al., 2021a) and the model in this work modelling the Tribet fuel with 5.3 MeV and specific α-activity of $4.73{\cdot}10^{8}$ Bq·g^{-1} with mass density 10.8 g.

consequently resulting in a lower average escape energy. This is also indicated in the discussion by the authors, where it is claimed that the empirical equation derived by Garisto overestimates the average escape energy. This is contrary to the results from this work, where it is shown that the higher mass stopping powers over the α-particle energy range from the work of Nitzki and Matzke leads to a lower escape energy. Furthermore, the α-particle range in the UO_2 matrix modelling the Tribet fuel is calculated in this work as 13.15 μm, which is the same as the value reported using the SRIM software of 13.2 μm (e.g. reported in the work of Poulesquen et al. (2006)). The corresponding value in the work of Siberry et al. is reported as 12.4 μm, which also indicate that the attenuation in the UO_2 material is overestimated.

The dissolution rate as a function of particle radius modelling the Tribet fuel is shown in Fig. 15. The figure clearly shows that the dissolution rate per surface area increases with particle size to asymptotically approach the value for a planar surface, while the dissolution rate per unit weight of UO_2-based material decreases with particle size. For very small radii the amount of H_2O_2 produced is proportional to the volume of the particle, which grows faster than the surface area with increasing radius, leading to a faster dissolution rate per unit surface area (Fig. 15a). However, this effect is counteracted when approaching larger radii due to the fact that the UO_2 matrix absorbs a significant fraction of the α-particle energy. Therefore, when expressing the dissolution rate per unit mass, the effect of the UO_2 matrix attenuating and absorbing significant fractions of the α-particles is very clear, with a sharply decreasing dissolution rate with increasing radius (Fig. 15b).

4. Conclusions

Dose rate calculations of spherical geometries are important for modelling the source term of radioactive particles existing due to nuclear waste, natural uranium deposits, severe nuclear accidents, or nuclear weapons testing. The current work expands both on the modelling of this geometry as well as on the crack geometries present in spent nuclear fuel due to the very high temperature gradients during operation.

A simplified continuous equation for the α-particle escape probability from spherical UO_2 particles was derived. The stepwise attenuation calculation of α-particles in the spherical UO_2 particles yielded escape probabilities that were closely predicted by the theoretical volume weighted escape probability equation. Despite higher escape probability as well as escape energy of the particles emitted from smaller particles, the dissolution rate analysis shows that the ratio between UO_2 particle volume able to irradiate surrounding solution and irradiated solution volume is an important factor in the interpretation of the results. This is well showcased by the conversion of the dose rates into area-specific dissolution rates.

The theoretical derivation of the isotropic emission of α-particles improved upon the previous model by our group. The main difference between the model in this work and the compared literature works can be accounted for by the difference in average particle emission energies in previous studies. The difference is likely due to an overestimation of the mass stopping power in the UO_2 matrix. This leads to a lower average particle escape energy as well as dose rate in the surrounding water layers. This indicates that the model developed in this work is an improvement to existing models in terms of calculating average escape energy and dose rate emitted from planar surfaces, cracks, and spherical particle geometries. The models presented in this work can be implemented in a variety of dose rate calculations as well as dissolution rate assessments.

Author statement

N.L. Hansson: Conceptualization, Data curation, Formal analysis, Investigation, Methodology, Software, Validation, Visualization, Original draft. M. Jonsson: Conceptualization, Methodology, Supervision,

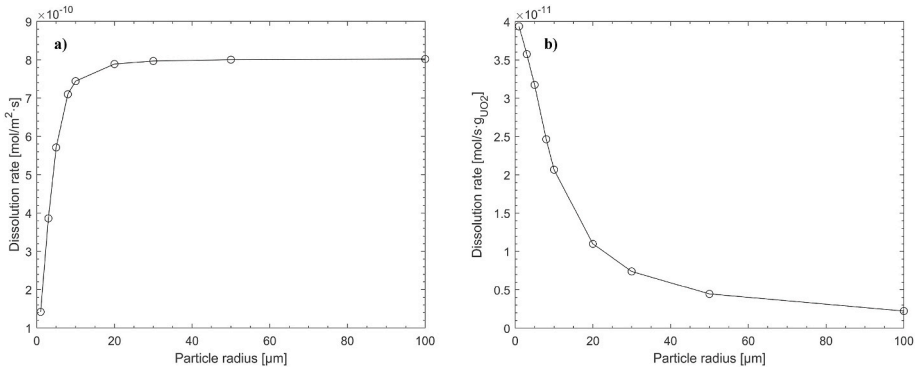

Fig. 15. –Area-specific (a) and weight specific (b) UO_2 dissolution rates modelling the Tribet fuel with UO_2 particles of radius 1–100 μm.

Validation, Review & editing. C. Ekberg: Funding acquisition, Resources, Supervision, Review & editing. K. Spahiu: Funding acquisition, Supervision, Review & editing.

Declaration of competing interest

The authors declare the following financial interests/personal relationships which may be considered as potential competing interests: Niklas L. Hansson reports financial support was provided by Swedish Nuclear Fuel and Waste Management Co.

Acknowledgements

The Swedish Nuclear Fuel and Waste Management Company, SKB, is gratefully acknowledged for funding of this project.(Funding number 24853).

References

Bauhn, L., Hansson, N., Ekberg, C., Fors, P., Delville, R., Spahiu, K., 2018. The interaction of molecular hydrogen with α-radiolytic oxidants on a (U,Pu)O_2 surface. J. Nucl. Mater. 505, 54–61. https://doi.org/10.1016/j.jnucmat.2018.04.006.

Christensen, H., 1998. Calculations simulating spent-fuel leaching experiments. Nucl. Technol. 124, 165–174. https://doi.org/10.13182/NT98-A2916.

Garisto, F., 1989. The energy spectrum of α-particles emitted from used CANDU™ fuel. Ann. Nucl. Energy 16, 33–38. https://doi.org/10.1016/0306-4549(89)90118-7.

Gregson, C.R., Goddard, D.T., Sarsfield, M.J., Taylor, R.J., 2011. Combined electron microscopy and vibrational spectroscopy study of corroded Magnox sludge from a legacy spent nuclear fuel storage pond. J. Nucl. Mater. 412, 145–156. https://doi.org/10.1016/j.jnucmat.2011.02.046.

Hansson, N., Ekberg, C., Spahiu, K., 2020. Alpha dose rate calculations for UO_2 based materials using stopping power models. Nucl. Mater. Energy 22, 100734. https://doi.org/10.1016/j.nme.2020.100734.

IAEA, 2011. Radioactive Particles in the Environment: Sources, Particle Characterization and Analytical Techniques. IAEA.

International Commission on Radiation Units, 1956. ICRU Report. International Commission on Radioation Units and Measurements.

Jansson, M., Jonsson, M., Eriksen, T., 1994. Basic model of geometrical dose distributions from small UO_2-particles. In: Swedish Nuclear Fuel and Waste Management Co. SKB U-96-44.

Jonsson, M., Nielsen, F., Roth, O., Ekeroth, E., Nilsson, S., Hossain, M.M., 2007. Radiation induced spent nuclear fuel dissolution under deep repository conditions. Environ. Sci. Technol. 41, 7087–7093. https://doi.org/10.1021/es070832y.

Kashparov, V.A., Ivanov, Y.A., Zvarisch, S.I., Protsak, V.P., Khomutinin, Y.V., Kurepin, A. D., Pazukhin, E.M., 1996. Formation of hot particles during the Chernobyl nuclear power plant accident. Nucl. Technol. 114, 246–253. https://doi.org/10.13182/NT96-A35253.

Mougnaud, S., Tribet, M., Rolland, S., Renault, J.-P., Jégou, C., 2015. Determination of alpha dose rate profile at the HLW nuclear glass/water interface. J. Nucl. Mater. 462, 258–267. https://doi.org/10.1016/j.jnucmat.2015.04.012.

Nielsen, F., Jonsson, M., 2006. Geometrical α-and β-dose distributions and production rates of radiolysis products in water in contact with spent nuclear fuel. J. Nucl. Mater. 359, 1–7. https://doi.org/10.1016/j.jnucmat.2006.08.001.

Nielsen, F., Lundahl, K., Jonsson, M., 2008. Simulations of H_2O_2 concentration profiles in the water surrounding spent nuclear fuel. J. Nucl. Mater. 372, 32–35. https://doi.org/10.1016/j.jnucmat.2007.01.279.

Nitzki, V., Matzke, H., 1973. Stopping power of 1-9-MeV He++ ions in UO_2,(U,Pu)O_2, and ThO_2. Phys. Rev. B 8. https://doi.org/10.1103/PhysRevB.8.1894, 1894.

Poulesquen, A., Jegou, C., Peuget, S., 2006. Determination of alpha dose rate profile at the UO_2/water interface. In: Mater. Res. Soc. Symp. Proc., p. 932. https://doi.org/10.1557/PROC-932-69.1.

Sattonnay, G., Ardois, C., Corbel, C., Lucchini, J., Barthe, M.-F., Garrido, F., Gosset, D., 2001. Alpha-radiolysis effects on UO_2 alteration in water. J. Nucl. Mater. 288, 11–19. https://doi.org/10.1016/S0022-3115(00)00714-5.

Shao, M.-Z., Badler, N., 1996. Spherical sampling by archimedes' theorem. Technical Reports (CIS) 184.

Shoesmith, D., 2000. Fuel corrosion processes under waste disposal conditions. J. Nucl. Mater. 282, 1–31. https://doi.org/10.1016/S0022-3115(00)00392-5.

Siberry, A., Hambley, D., Adamska, A.M., Springell, R., 2021a. A geometrical model to describe the alpha dose rates from particulates of UO_2 in water. Radiat. Phys. Chem. 188 https://doi.org/10.1016/j.radphyschem.2021.109677, 109677.

Siberry, A., Hambley, D., Adamska, A., Springell, R., 2021b. A mathematical model to describe the alpha dose rate from a UO_2 surface. Radiat. Phys. Chem. 182, 109359 https://doi.org/10.1016/j.radphyschem.2021.109359.

Sunder, S., 1998. Calculation of radiation dose rates in a water layer in contact with used CANDU UO_2 fuel. Nucl. Technol. 122, 211–221. https://doi.org/10.13182/NT98-A2863.

Toftegaard, J., Lühr, A., Sobolevsky, N., Bassler, N., 2014. Improvements in the stopping power library libdEdx and release of the web GUI dedx. au. dk. In: J. Phys. Conf. Ser. IOP Publishing, 012003. https://doi.org/10.1088/1742-6596/489/1/012003.

Tribet, M., Mougnaud, S., Jégou, C., 2017. Spent nuclear fuel/water interface behavior: alpha dose rate profile determination for model surfaces and microcracks by using Monte-Carlo methods. J. Nucl. Mater. 488, 245–251. https://doi.org/10.1016/j.jnucmat.2017.03.027.

Vilks, P., Cramer, J., Bachinski, D., Doern, D., Miller, H., 1993. Studies of colloids and suspended particles, Cigar Lake uranium deposit, Saskatchewan, Canada. Appl. Geochem. 8, 605–616. https://doi.org/10.1016/0883-2927(93)90016-A.

Weisstein, E.W., 2007. Sphere-sphere Intersection. https://mathworld.wolfram.com/.

Zheltonozhsky, V., Mück, K., Bondarkov, M., 2001. Classification of hot particles from the Chernobyl accident and nuclear weapons detonations by non-destructive methods. J. Environ. Radioact. 57, 151–166. https://doi.org/10.1016/s0265-931x(01)00013-3.

Ziegler, J.F., Ziegler, M.D., Biersack, J.P., 2010. SRIM–The stopping and range of ions in matter. Nucl. Instrum. Methods Phys. Res. B: Beam Interact. Mater. At. 268, 1818–1823. https://doi.org/10.1016/j.nimb.2010.02.091, 2010.